Verdon, J., & Budge, J. (2018). Examining the Capability of Statistical Models to Mitigate Induced Seismicity during Hydraulic Fracturing of Shale Gas Reservoirs. *Bulletin of the Seismological Society of America*, *108*(2), 690-701. https://doi.org/10.1785/0120170207

Examining the capability of statistical models to mitigate induced seismicity during hydraulic fracturing of shale gas reservoirs

James P. Verdon[1*], Jessica Budge[2]

1. School of Earth Sciences, University of Bristol, Wills Memorial Building, Queen's Road, Bristol, U.K., BS8 1RJ.

2. Nexen Energy ULC, 801 7th Avenue SW, Calgary, AB, Canada, T2P 3P7.

* Corresponding Author. Email: James.Verdon@bristol.ac.uk, Tel: 0044 117 331 5135.

ABSTRACT

Injection into the subsurface is carried out by industry for a variety of reasons: storage of waste-water; enhanced oil recovery; and for hydraulic fracture stimulation. By increasing subsurface pressures, injection can trigger felt seismicity (i.e. of sufficient magnitude to be felt at the surface) on pre-existing faults. As the number of cases of felt seismicity associated with hydraulic fracturing has increased, strategies for mitigating induced seismicity are required. However, most hydraulic stimulation activities do not induce felt seismicity. Therefore a mitigation strategy is required that is capable of differentiating the "normal" case from "abnormal" cases that trigger larger events. In this paper we test the ability of statistical methods to estimate the largest event size during stimulation, applying these approaches to two datasets collected during hydraulic stimulation in the Horn River Shale, British Columbia, where hydraulic fracturing was observed to reactivate faults. We apply these methods in a prospective manner: using the microseismicity recorded during the early phases of a stimulation stage to make forecasts about what will happen as the stage continues. We do so to put ourselves in the shoes of an operator or regulator, where decisions must be taken based on data as it is acquired, rather than a post hoc analysis once a stimulation stage has been completed. We find that the proposed methods can provide a reasonable forecast of the largest event to occur during each stage. This means that these methods can be used as the basis of a mitigation strategy for induced seismicity.

INTRODUCTION

Hydraulic Fracturing-Induced Seismicity

Any human activity that alters the stress state in the Earth's crust has the potential to induce seismic activity. Induced seismicity has been associated with: mining (e.g., Li et al., 2007); impoundment of reservoirs (e.g., Gupta, 1985); conventional oil and gas extraction (e.g., Segall, 1989); and subsurface fluid injection, whether for hydraulic fracturing (e.g., Bao and Eaton, 2016), disposal of waste fluids (e.g., Keranen et al., 2013), Carbon Capture and Storage (e.g., Stork et al., 2015), or geothermal energy (e.g., Häring et al., 2008).

It has been conclusively demonstrated that injecting fluids into the subsurface can trigger seismicity, where increased pore-fluid pressures lead to the activation of critically-stressed faults (e.g., Raleigh et al., 1976). However, it should be noted that the overwhelming majority of such operations are not thought to cause earthquakes. Nevertheless, as the above practices have increased in scale and become more widespread, the issue of injection-induced seismicity has grown in significance.

While much of the recent focus has been on waste-water disposal, several cases of hydraulic fracturing-induced seismicity (HF-IS) have been identified (e.g., B.C. Oil and Gas Commission 2012, 2014; Clarke et al. 2014; Friberg et al., 2014; Darold et al., 2014; Skoumal et al., 2015; Schultz et al. 2015a,b; Atkinson et al., 2016; Bao and Eaton, 2016; Wang et al., 2016). It is vital that our understanding of HF-IS improves, such that industrial operators are capable of mitigating against triggering seismic activity. However, for many of these case examples monitoring arrays were not deployed until after large events had occurred, or available monitoring arrays consisted solely of regional networks, where the nearest station may have been many km from the site. This means that there is often little useful data that can be used to study the processes that happened in the lead-up to these events, and thereby what mitigation steps might have been possible.

The number of cases of HF-IS is very small when compared to the overall number of wells that have been hydraulically stimulated. As such, any mitigation scheme should be capable of quickly differentiating the "normal case", where hydraulic fracturing does not cause fault re-activation leading to larger events, from the "abnormal case" where large events may be triggered, and therefore where mitigating strategies, such as reducing injection volumes or ceasing injection altogether, may be necessary.

Mitigation of HF-IS

At present, where regulations pertaining to HF-IS have been applied, they have taken the form of Traffic Light Schemes (TLSs), whereby operators take actions based on the magnitude of events induced during operations. These schemes have the advantage of being relatively simple to administer, and can be understood by the public. However, there are somewhat reactive in their nature (as opposed to proactive): an operational response is required, such as reducing or stopping injection, only after an event of a given size has occurred.

The purpose of this paper is not to argue against the use of TLSs, which can play a useful role in the regulation of HF-IS. However, it is our view that, in addition to complying with TLS regulations, operators should seek to mitigate induced seismicity in a more proactive manner. If nothing else, operators will wish to ensure that they remain within the specified TLS thresholds during their operations, since reaching "red lights" entails the imposition of operational constraints, and may also affect operator reputation and confidence with the public.

To take a proactive approach to HF-IS, operators must develop the capacity to model their activities, allowing them to make forecasts about the HF-IS that may occur as their operations continue. In the broadest sense, two types of modelling approach are available: physical and statistical. Physical models aim to simulate the processes that occur during hydraulic stimulation, usually using numerical methods such as finite elements (e.g. Maxwell et al., 2015), discrete elements (e.g., Yoon et al., 2014), rate and state approaches based on

84 modelled stress changes (e.g., Hakimhashemi et al., 2014), or by resolving modelled stress
85 changes onto pre-existing fault/fracture networks (e.g., Verdon et al., 2015). However, such
86 models often require extensive site characterisation to identify and characterise both nearby
87 faults and the local stress state. Such models also come with a significant number of free
88 parameters that must be "tuned" to provide a reasonable representation of reality. As such
89 they are better suited for understanding the physical processes that have occurred at a site *a*
90 *posteriori*. For hydraulic fracturing operators who might be required to manage induced
91 seismicity in real time at a significant number of active well sites, simple models with a
92 relatively small number of free parameters are required. In this respect, statistical models
93 become more favourable.

94 Statistical approaches seek to characterise the observed seismic event population via a
95 statistical model, usually the Gutenberg and Richter (1944) (G-R hereafter) distribution. Such
96 a model can then be extrapolated to estimate the event population that is expected to have
97 occurred by the end of the injection period. Several such models have been proposed, for
98 example: Shapiro et al. (2010); McGarr (2014); Hallo et al. (2014); and van der Elst et al.
99 (2016).

100 These models are similar in their underlying assumptions: event magnitudes can be
101 characterised by the G-R distribution, and the rate of seismicity is linked in some way to the
102 injection volume. This relationship is then extrapolated based on recorded seismicity during
103 the early stages of injection to estimate what the resulting event population would be once the
104 total volume has been injected. From this estimated population, the largest event size can be
105 forecast. These models have the advantage that they require only a few parameters, which can
106 be measured as operations progress. This makes them better-suited for the task of providing *a*
107 *priori* mitigation of induced seismicity.

108 While these models have been tested at several sites (e.g. Hallo et al., 2014; Hajati et al.,
109 2015), the crucial aspect investigated in this paper is that we seek to apply these methods in a
110 prospective manner (e.g. Langenbruch and Zoback, 2016). We do not apply these models

111 using the overall event population that has been acquired during hydraulic stimulation in a
112 *post hoc* manner. Instead, we put ourselves into the shoes of an operator or regulator, where
113 forecasts must be made using only the data that has been acquired prior to a given point in
114 time. Evidently, the underlying assumption for these methods is that the parameters used to
115 characterise the seismicity as a function of injection volume remain unchanged during a given
116 operation.

117 We apply these methods to two datasets collected during hydraulic stimulation in the Horn
118 River Shale. These multi-well, multi-stage sites were monitored using downhole
119 microseismic arrays, producing very high quality datasets. These datasets are described in the
120 following section, after which we describe the methods of Shapiro et al. (2010) and Hallo et
121 al. (2014) in greater detail, and apply them to the datasets.

122 DATASETS

123 In our case example we examine microseismic datasets from two multi-well, multi-stage
124 hydraulic fracturing treatments conducted in the Horn River Shale formation in British
125 Columbia, Canada. The pads from which the two sets of wells were drilled are approximately
126 7km apart from each other. In the following we refer to the two datasets as HR1, which was
127 completed in 2011, and HR2, which was completed in 2013. These datasets were provided by
128 the operating company: they are proprietary and cannot be released to the public.

129 HR1 Microseismic Data

130 A total of 9 horizontal wells were drilled from the HR1 pad. A total of 146 stages were
131 stimulated, with between 15 – 18 stages per well. Microseismic data was recorded by arrays
132 of up to 100 3-component geophones placed in boreholes adjacent to those being stimulated
133 (in both the vertical and horizontal sections of the wells). The positions of the geophones
134 were varied as stimulation progressed along the wells, in at least 21 configurations.

Data were provided from 76 of the stages, consisting of a total of 140,100 events. These were the stages closest to the heels of the wells, and therefore closest to the monitoring arrays, where the best quality microseismic data could be gathered. Events were located by inverting picked P- and S-wave arrival times through a layered, anisotropic velocity model. A map and cross-section of the HR1 microseismic events are shown in Figure 1. Event magnitudes were calculated by fitting an idealised source model to the event displacement spectra to determine the seismic moment (e.g., Stork et al., 2014). Throughout this paper, when referring to "magnitude" our implication is moment magnitude, M_W. In both cases this processing of the data was performed by a service provider, ESG Solutions.

HR2 Microseismic Data

A total of 10 wells were drilled from the HR2 pad. 237 stages were stimulated, with between 23 – 24 stages per well. Microseismic data was recorded by an array of 96 3-component geophones placed in 3 adjacent boreholes. Data was provided from 119 stages, consisting of 92,700 events. As with the HR1 pad, data was provided for the stages nearest to the heels of the wells, where they are in closest proximity to the monitoring array (and therefore are expected to provide the best quality data). A map and cross-section of the HR2 events are shown in Figure 2.

In both case studies, examination of event locations reveals evidence for the interaction between hydraulic fracturing and faults in the form of planar features extending downwards into the underlying Keg River limestone formation. At HR1, the largest event has a magnitude of $M_W = 1.3$, while at HR2 the largest event has a magnitude of $M_W = 0.5$. In both cases, these magnitudes are larger than what is typically observed when hydraulic fractures propagate through shale gas reservoirs, where magnitudes are generally less than 0 (e.g., Maxwell et al., 2010).

USING EVENT POPULATION STATISTICS TO FORECAST THE LARGEST EVENT SIZE

In the following sections, we refer to M^{O}_{MAX} as the largest magnitude event *observed* during a particular stage, and M^{M}_{MAX} as the expected largest magnitude as estimated by a *modelling* strategy. Ideally, modelling strategies should aim to produce conservative estimates of M^{M}_{MAX}, such that $M^{O}_{MAX} \leq M^{M}_{MAX}$. Here we examine the abilities of two published methods, Shapiro et al. (2010) and Hallo et al. (2014), to forecast M^{M}_{MAX} during hydraulic stimulation.

Seismogenic Index, Shapiro et al. (2010)

Shapiro et al. (2010) define the Seismogenic Index, S_I as

$$S_I = \log_{10}\left(\frac{N_t(M)}{V_t}\right) + bM, \quad (1)$$

where $N_t(M)$ is the number of events that have occurred at time t that are larger than a given magnitude M, b is the G-R b-value for the observed event magnitude distribution (EMD), and V_t is the cumulative volume injected up until this time (note that Shapiro et al. (2010) use Σ to denote the seismogenic index: we use S_I instead to differentiate with other uses of Σ elsewhere in this paper). Assuming that the number of events induced per unit volume injected does not change, then S_I will be constant: constant S_I has been observed by Dinske and Shapiro (2013) and van der Elst et al. (2016) for a wide range of cases studies. Shapiro et al. (2010) show that, in such an instance, if the occurrence of individual events can be treated as an independent Poisson process, then the probability that an event larger than M does not occur if a total volume V_T is injected can be calculated as

$$\mathbb{P} = \exp\left(-V_T . 10^{S_I - bM}\right). \quad (2)$$

Re-arranging this equation, we arrive at a forecast for the size of event that will not be exceeded, given a confidence level χ:

$$M^{M}_{MAX} = \left(S_I - \log\left(\frac{-\ln(\chi)}{V_T}\right)\right)/b. \quad (3)$$

In order to provide a mitigation strategy, we are interested in establishing an upper bound for M_{MAX}, i.e., to establish what size of earthquake will not occur (or is unlikely to occur).

Therefore, for the entirety of this study we consider the upper bound of the distribution described by Shapiro et al. (2010), setting $\chi = 0.95$.

Seismic Efficiency, Hallo et al. (2014)

McGarr (2014) proposed that the cumulative seismic moment released during injection, ΣM_O, is determined by the total cumulative volume of fluid injected:

$$\Sigma M_O = 2\mu V_T, \tag{4}$$

where μ is the rock shear modulus. However, this equation can be considered as a worst-case scenario, where all the strain induced by a volume change is released as seismic energy. In reality, much of the deformation induced by injection will be released aseismically. Hallo et al. (2014) therefore define a seismic efficiency ratio, S_{EFF}, which describes the ratio of observed cumulative moment release to the theoretical maximum given by μV_T. Equation 3 is thereby modified to:

$$\Sigma M_O = S_{EFF}\mu V_T, \tag{5}$$

where S_{EFF} can be estimated at a given time from the cumulative moment release and the cumulative injected volume up until this time.

For a given cumulative seismic moment release, size of the largest event will be determined by the b value. Hallo et al. (2014) show that ΣM_O can be related to the b value, and the largest event detected, M^M_{MAX}, and the minimum magnitude of completeness, M_{MIN}:

$$\Sigma M_O = \frac{b.10^a.10^{9.1}}{1.5-b}\left(10^{\left(M^M_{MAX}(1.5-b)\right)} - 10^{\left(M_{MIN}(1.5-b)\right)}\right), \tag{6}$$

where

$$a = bM^M_{MAX} - \log\left(10^{b\delta} - 10^{-b\delta}\right), \tag{7}$$

and δ is the probabilistic half-bin size defined around M^M_{MAX}, as described by Hallo et al. (2014). Based on equation 5, we can determine the total expected ΣM_O based on the observed seismic efficiency S_{EFF} and the planned total injection volume V_T. Once we have estimated

ΣM_O, we invert equations 6 and 7 to forecast M^M_{MAX} based on the observed b values. Essentially, M^M_{MAX} is a function of the seismic efficiency, which describes how much seismic moment is released per unit volume injected, and the b value, which describes whether this seismic moment is released as a few large events or as many small events.

Whereas the Shapiro et al. (2010) S_I method provides a probability distribution for M_{MAX} (Equation 3), the Hallo et al. (2014) method provides a single estimate for M^M_{MAX} based on the observed (or forecast) b and S_{EFF} values. As such, assuming the Hallo et al. method is a true representation of the induced seismicity, random variability alone would mean that the actual M^O_{MAX} value would be larger than the model for half the cases. As described above, our aim is to establish conservative M^M_{MAX} values, whereby we have confidence that no events larger than M^M_{MAX} will occur. Therefore we require a value based on equations 6 and 7 that also takes into account uncertainties inherent in the approach.

To do this we consider synthetic, stochastically generated event populations. By randomly sampling from a G-R distribution, we generate event populations with a given b value and ΣM_O chosen randomly from $0.8 < b < 3.5$ and $9 < \log_{10} \Sigma M_O < 14$. We then compare the largest sampled event (which we refer to as the "synthetic M^O_{MAX}") with that forecast from the given b and ΣM_O values using equations 6 and 7 (the "forecast M^M_{MAX}"). Our results for 1,000 such realisations are shown in Figure 3. We find that for 98% of model realisations, the forecast value of M^M_{MAX} is within 0.5 magnitude units of the synthetic M^O_{MAX}. Because we are primarily concerned with setting a conservative envelope that is not exceeded, in the following sections we take as M^M_{MAX} the value computed using the Hallo et al. method (equations 6 and 7) + 0.5.

There is currently some debate as to whether there really is a link between injection volume and the rate and/or size of induced earthquakes (e.g. Atkinson et al., 2016; van der Elst et al., 2016). This debate stems from fundamental questions as to the nature of rupture mechanics during induced seismicity. Gischig (2015) describes two end-members for rupture behaviour. In the first case rupture may initiate within the zone of increased pressure, but uncontrolled

rupture can continue along faults outside of this zone, releasing tectonically-accumulated strain energy. Event size will be therefore determined by tectonic factors such as fault dimensions and *in situ* stress conditions. In the second case the rupture is spatially limited to the zone of increased pore pressure, in which case the injection volume places an *a priori*, deterministic limit on the maximum event size.

The second case, where the injection volume places a deterministic limit on event size, is often characterised by the McGarr (2014) limit (Equation 4). However, observations of events that appear to breach this limit (e.g., Atkinson et al., 2016) indicate that, at least in certain cases, the first of the Gischig (2015) end-members applies. Therefore an *a priori* deterministic limit on event size cannot be assumed based on injection volume.

However, in our approach there is no requirement that $S_{EFF} \leq 1$, and therefore there is no *a priori* deterministic limit to event size. If $S_{EFF} > 1$, this indicates that the cumulative moment released is larger than the strain energy introduced by injection, and therefore that tectonically accumulated strain energy is also being released. Equation (5) requires simply that there is proportionality between V_T and ΣM_O, where S_{EFF} is to be determined by observation for a given site. Van der Elst (2016) examined a range of case studies to investigate whether the number of earthquakes induced during injection is proportional to injection volume, and found strong evidence that this was indeed the case, with the implication that the event nucleation rate is controlled by the injection volume. If b values are constant, then this implies that the cumulative moment release will also be proportional to injection volume.

Application to microseismic data

To compute b values we use the maximum likelihood approach described by Aki (1965). To estimate M_{MIN}, we follow the method described by Clauset et al. (2009) to assess the quality of fit between the observed EMD and the G-R relationship using a Kolmogorov-Smirnov test, choosing as M_{MIN} the smallest magnitude at which the null hypothesis (that the observed distribution can be modelled by the G-R relationship) is not rejected at a 10% significance

level. Fitting a G-R relationship to an observed EMD can be unreliable for low event numbers. Therefore we require a minimum of 50 events with magnitudes larger than M_{MIN} for a reliable measurement. This means that our approach will only provide an estimate for M^M_{MAX} once sufficient microseismic events have occurred.

Figure 4 shows an example of how we apply these methods to the microseismic datasets. Plots for every stage are available in the supplementary materials. We proceed at intervals of 120 seconds. After each interval has elapsed, we re-calculate the b, S_{EFF}, and S_I parameters based on the total volume injected and the events recorded up until this time. We then use equations 3, 6 and 7 to estimate, using the Shapiro et al. (2010) and Hallo et al. (2014) methods, the expected value of M^M_{MAX} given the injection volume that is planned to take place during the next 120s interval.

In the lower panel of Figure 4, we plot the measured values of b, S_{EFF}, and S_I with time. In the upper panel of Figure 4 we compare the resulting forecasts of M^M_{MAX} with observed event magnitudes. We note that in the example shown in Figure 4, the forecast largest event size stabilizes at a value of approximately $M^M_{MAX} = 0.2$ within 40 minutes of the start of injection. This is slightly larger than the largest observed event, which has a magnitude of $M^O_{MAX} = 0.0$ and occurs 140 minutes after the start of injection.

In the following sections we compare M^O_{MAX} with the value of M^M_{MAX} at the time that the largest event occurred. We also compare M^O_{MAX} with M^M_{MAX} at a time 60 and then 30 minutes before the largest event occurred. We do this to identify the capacity of such methods to provide an opportunity for mitigation by giving an operator sufficient warning to alter (or cease) their stimulation program.

Before considering the results of our method as applied to all stages of both datasets, we note several features from Figure 4. Firstly, we note the similarity between the two curves for S_I and $\log_{10}(S_{EFF})$. This is to be expected given how the two parameters are defined. If M_{MIN} is used as the "M" term in equation 3, then the difference $S_I - \log_{10}(S_{EFF})$ will be given by:

$$S_I - \log S_{EFF} = \log(N_t(M_{MIN})/V_t) + bM_{MIN} - \log(\Sigma M_O/\mu V_t). \quad (8)$$

Rearranging this equation, and substituting $\Sigma M_O = N_t \langle M_O \rangle$, where $\langle M_O \rangle$ is the mean moment release per event, we get

$$S_I - \log S_{EFF} = bM_{MIN} - \log(\langle M_O \rangle/\mu). \quad (9)$$

In the case studies presented here, M_{MIN} is typically approximately -1.5, b is typically 2, $\langle M_O \rangle$ is typically of the order 10^7 Nm (equivalent to a magnitude of approximately -1) and we approximate the shear modulus as $\mu = 20\text{x}10^9$ Pa. Hence the similarity in values between S_I and $\log_{10}(S_{EFF})$. We also note that the values of M^M_{MAX} computed by the two methods are similar. This gives us confidence that both independent methods are providing similar results.

RESULTS

Before showing the results using the two methods described above, in Figure 5 we compare the observed values for M^O_{MAX} for each stage with the values of M^M_{MAX} forecast using the McGarr (2014) equation $M^M_{MAX} = \mu V_T$. We do this primarily to demonstrate that there does not appear to be any correlation between the observed M^O_{MAX} of each stage and the volume injected at the time of occurrence of each event. We also note that the observed magnitudes are far smaller than those estimated by the McGarr (2014) equation.

In Figure 6 we compare the observed and forecast M_{MAX} values using the Hallo et al. (2014) method. As per Figure 4, we compare the forecast M^M_{MAX} values at the time that the largest event occurred, but also compare the forecast M^M_{MAX} values 30 and 60 minutes before the occurrence of the largest event. In Figure 7 we do the same for the Shapiro et al. (2010) method.

We note several features from these results. Firstly, as required, in general $M^M_{MAX} \geq M^O_{MAX}$ for almost every stage. Not only this, but stages that produced smaller events have smaller values of M^M_{MAX}, *id est* there is clear correlation between M^M_{MAX} and M^O_{MAX}. This is encouraging, as it implies that these methods do have some forecasting power, unlike the results provided by

313 the McGarr (2014) approach shown in Figure 5. This correlation is present even for the T –
314 60mins measurements, implying that these methods are capable of identifying stages that may
315 induce larger events a significant period of time before such events occur.

316 There is only 1 stage, at HR2, where both the Shapiro et al. (2010) and Hallo et al. (2014)
317 methods significantly underestimate M^{O}_{MAX}. We note that this stage had only 131 events in
318 total, making it one of the smallest stages in terms of the number of events. The robustness of
319 statistical techniques such as these will be dependent on the number of events sampled, so it
320 is perhaps unsurprising that stages with fewer events might produce less reliable results.

321 DISCUSSION

322 Do seismicity parameters vary during injection stages?

323 The models we use to forecast M^{M}_{MAX} are entirely statistical, and do not incorporate any
324 geological information. The major advantage of these statistical approaches is that they are
325 relatively simple to use (requiring only that the volume injected, and the number and
326 magnitude of seismic events can be measured). The principal assumption that underpins this
327 type of approach is that both b, S_{EFF} and/or S_I will remain consistent throughout the injection
328 period. It is by no means clear that this will always be the case.

329 These parameters might be affected by a range of factors including: the *in situ* stress
330 conditions; the lithology of the rock through which hydraulic fractures are propagating; and
331 the presence of pre-existing fracture networks and/or faults. Generally speaking, the volume
332 of rock influenced by injection increases as the pressure front moves out from the injection
333 well. Therefore, the pressure pulse induced by injection may begin to act on different layers
334 and/or structures as injection continues. It is easy to imagine scenarios where a growing
335 hydraulic fracture intersects with a pre-existing fault, or propagates into an under- or
336 overlying layer that is more seismogenic, resulting in a change in the rate of seismicity and/or
337 b value.

The key question then becomes whether such changes are rapid, or whether there will be a more gradual evolution. If the seismicity changes suddenly then larger events may occur that cannot be anticipated based on the preceding microseismicity. It would therefore be very difficult for an operator to mitigate induced seismicity, as larger events would occur "out of the blue". In contrast, if such changes occur relatively gradually then an operator may be able to identify an increase in the seismicity rate, or a decrease in the G-R *b*-value, that would indicate an increasing probability of a larger event occurring. If closely monitored, this might allow an operator to take appropriate mitigating action (reducing pumping rates and/or pressures, or indeed ceasing to pump altogether).

Incidentally, this assumption is also implicit in existing schemes that are used to mitigate induced seismicity, such as TLSs, although this assumption is rarely stated explicitly. If large events are triggered immediately when a HF intersects a fault, then TLSs will be ineffective, because an event that is much larger than the red-light threshold could occur without any prior TLS-based mitigation actions having been taken. In contrast, if there is a more gradual build-up of seismicity upon intersection between a hydraulic fracture and a fault, then the amber and red lights will progressively be triggered, and the appropriate mitigation steps taken.

We note that both Dinske and Shapiro (2013) and van der Elst et al. (2016) have observed remarkably constant values of S_I during fluid injection, across a wide variety of settings including hydraulic fracturing, stimulation of geothermal reservoirs, and during wastewater disposal. There are also sound physical reasons to expect a gradual increase in seismic magnitudes as a hydraulic fracture impinges on a fault, as opposed to a sudden "jump". When a fracture first meets a fault, both the area of the fault affected, and the volume of fluid injected into the fault will be small. As such, we might expect the initial events to be smaller. As injection continues, the area of the fault affected will increase, as will the volume of fluid injected into it, which would be expected to increase the event magnitudes as injection continues.

365 This assumption is borne out in the results we present here, most notably in the fact that the
366 forecast M^{M}_{MAX} values tend to anticipate the observed largest events by at least 60 minutes
367 (Figures 6 and 7). It is also apparent when the evolution of these parameters is examined in
368 detail during each stimulation stage (see supplementary material). The implication is that
369 large induced events do not occur "out of the blue", but are accompanied by a build-up in
370 seismicity as the stimulation impinges on a pre-existing fault.

371 **Strategy for Mitigation of Induced Seismicity**

372 Based on the above results, we suggest the following strategy for the mitigation of induced
373 seismicity. Prior to the start of operations, an acceptable threshold for M^{M}_{MAX} is set, based on
374 the vulnerability of nearby populations, buildings and infrastructure to seismic activity, and
375 the expected ground motion that would be caused by events of a given size.

376 In this case, we arbitrarily set our thresholds as $M^{M}_{MAX} > 1$. Given the relative lack of
377 buildings, local populations or infrastructure near to this site, this is a relatively conservative
378 threshold, but nevertheless affords a clear demonstration of the approach. Because the results
379 for the Hallo et al. (2014) method show a tighter correlation between M^{M}_{MAX} and M^{O}_{MAX} (c.f.
380 Figures 6 and 7), we use this approach as our preferred method to compute M^{M}_{MAX}. If M^{M}_{MAX}
381 exceeds this threshold during a stage, then mitigating actions should be taken. In this case we
382 suggest that the mitigating action would be to cease injection and move on to the next stage.

383 Based on our results, we divide the stages into 3 categories: stages where the $M^{M}_{MAX} > 1$
384 threshold is never reached and therefore no mitigation action is indicated (Figure 8a,b); stages
385 where the $M^{M}_{MAX} > 1$ threshold is reached only after the occurrence of the largest observed
386 event (Figure 8c,d); and stages where the $M^{M}_{MAX} > 1$ threshold is reached before the
387 occurrence of the largest event (Figure 8e,f).

388 The first category of stages, where the $M^{M}_{MAX} > 1$ threshold was not exceeded at any time, is
389 represented in Figure 8a. An example of such a stage is shown in Figure 8b. 159 out of 195
390 total stages (82%) fall into this category. The circles in Figure 8a show the largest event to

391 occur in each of these stages: the largest event to occur in a stage where the $M^M_{MAX} > 1$
392 threshold was not reached had a magnitude of $M_W = 0.4$.

393 The second category of stages is where the $M^M_{MAX} > 1$ threshold was exceeded, but only after
394 the occurrence of the largest event (Figure 8c). An example of such a stage is shown in Figure
395 8d: in this stage the largest event, which has a magnitude of $M^O_{MAX} = 0.58$, occurs after
396 approximately 1 hour. The $M^M_{MAX} > 1$ threshold is reached after 2 hours of injection. Because
397 the threshold is reached after the occurrence of the largest event, any mitigation steps that
398 might have been taken would not affect the size of largest event to occur during these stages.
399 A total of 16 stages (8%) fall into this category, and M^O_{MAX} for each of these stages is
400 depicted in Figure 8c. The largest magnitude event to occur during these stages had a
401 magnitude of $M_W = 0.88$.

402 The third category of stages is where the $M^M_{MAX} > 1$ threshold was exceeded prior to the
403 occurrence of the largest event. An example of such a stage is shown in Figure 8f: in this
404 stage the $M^M_{MAX} > 1$ threshold is reached after approximately 1 hour of injection. This is over
405 2.5 hours before the occurrence of the largest event, which had a magnitude of $M^O_{MAX} = 1.24$.
406 In other words, the potential for an $M_W > 1$ event is identifiable at a relatively early point
407 during the stage, and it is therefore possible that actions could have been taken that might
408 have mitigated the occurrence of this event. A total of 20 stages (10%) fall into this third
409 category, where the $M^M_{MAX} > 1$ threshold was reached prior to the occurrence of the largest
410 event. These stages are depicted in Figure 8e, where the squares indicate the size of the
411 largest event to occur prior to reaching the $M^M_{MAX} > 1$ threshold, while triangles indicate the
412 eventual largest event to occur. Within this category of stages, three had events with
413 magnitudes larger than $M_W = 1$. However, the largest event to occur before reaching the
414 $M^M_{MAX} > 1$ threshold had a magnitude of $M_W = 0.65$.

415 Overall, we note that for all the stages where the largest event was smaller than $M^O_{MAX} < 0$, no
416 mitigation actions were indicated. For some stages where $0 < M_W < 1$ mitigation actions were
417 indicated, while in others they were not. For all the stages where the largest event exceeded

418 $M^{O}_{MAX} > 1$, mitigation actions were always indicated prior to the occurrence of these events.
419 The result is that, for our "mitigated" population there are no stages where the largest event
420 exceeds $M_W > 1$.

421 **Mitigating actions and post-injection seismicity**

422 The major caveat that applied to the results described above is the assumption that ceasing
423 injection can prevent the subsequent larger events from happening. In reality injection was
424 not stopped, and so we cannot know whether cessation of injection during a stage would
425 actually have mitigated the larger events that occurred later in the stage. In other cases of
426 induced seismicity, events have continued with increasing magnitudes even after injection
427 had ceased (e.g., Häring et al., 2008). It is certainly possible that this would have been the
428 case at this site. Therefore it is not possible to definitively conclude that, even if mitigation
429 steps had been taken, further seismicity would not have occurred. Nevertheless, we believe
430 that it is important that operators develop scientific criteria to guide operational decisions
431 with respect to mitigating induced seismicity, and that the results presented here clearly
432 indicate that the methods described in this paper do provide such a basis.

433 ## CONCLUSIONS

434 We have presented case studies from two sites where microseismic monitoring has imaged
435 pre-existing faults being activated during hydraulic fracturing. We investigate the use of two
436 statistical methods found in the literature (Shapiro et al., 2010; Hallo et al., 2014) to forecast
437 the largest event size that might be expected during a hydraulic fracturing stage. The basis of
438 these two methods is to characterise the rate of seismicity with respect to the injection
439 volume, and thereby extrapolate to an expected event distribution once the planned total
440 volume has been injected.

441 Rather than examining these case studies *post hoc*, we explore the potential of these methods
442 to work in a prospective manner: at each given time-step we only make use of information

that is available prior to this time. We do this to put ourselves in the shoes of an operator or regulator, where decisions must be taken in real time as injection proceeds. We find that the proposed methods can forecast the largest event magnitudes with a reasonable degree of accuracy. This enables us to propose a strategy to mitigate HF-IS, whereby alterations to the injection strategy should be made if M^{M}_{MAX} exceeds a given threshold. We show that this strategy may have been able to mitigate the larger events that occurred at our case study sites.

The underlying assumption for these methods is that the rate of seismicity with respect to the injection volume will not alter during injection, or that if a fault is encountered, it will evolve gradually, allowing mitigation actions to be taken if real-time monitoring is used. We find that this assumption appears to hold for the datasets considered here. However, further study is required to examine whether this is the case more generally. This highlights the need for good quality seismic monitoring if the science around injection-induced seismicity is to advance. In many of the most well-known case examples, local monitoring arrays were only installed after the largest events had occurred. It is therefore difficult to determine with any certainty what happened in the time leading up to the triggering, and whether an operator could have made observations that in turn might have allowed them to take mitigating actions.

The most effective types of monitoring system are either downhole arrays (e.g., Maxwell et al., 2010), as per both case studies in this paper, or Very Large, Very Dense (VLVD) surface arrays, over which data are migrated and stacked (e.g., Chambers et al., 2010). Unfortunately, the costs of these types of deployment are high, and it is unlikely that such systems will be deployed at every injection project. However, novel processing methods using smaller arrays of seismometers placed at the surface (e.g., Skoumal et al., 2015; Verdon et al., 2017) are being used to improve the quality of datasets available.

Injection induced seismicity is a growing concern for various industries, and regulators are increasingly requiring operators to deploy monitoring arrays, usually to meet a traffic light scheme requirement of some form. We anticipate that, as more case studies become available,

our understanding of injection induced seismicity will grow, and our ability to mitigate such events will thereby improve.

Data and Resources

The datasets presented in this paper were acquired by the operating company, and are proprietary. Therefore they cannot be released to the public.

Acknowledgements

The authors would like to thank the operator of these Horn River sites for allowing us to access the data, and to acknowledge ESG Solutions Ltd., the microseismic service provider who processed the dataset. We would also like to thank the sponsors of the Bristol University Microseismicity Project (BUMPS), under whose auspices this work was performed.

References

Aki, K., 1965, Maximum likelihood estimate of b in the formula log $N = a - bM$ and its confidence limits: Bulletin of the Earthquake Research Institute, University of Tokyo 43, 237-239.

Atkinson G.M., Ghofrani H., Assatourians K., 2015. Impact of Induced Seismicity on the Evaluation of Seismic Hazard: Some Preliminary Considerations: Seismological Research Letters 86, 1009-1021.

Atkinson G.M., Eaton D.W., Ghofrani H., Walker D., Cheadle B., Schultz R., Shcherbakov R., Tiampo K., Gu J., Harrington R.M., Liu Y., van der Baan M., Kao H., 2016. Hydraulic fracturing and seismicity in the Western Canada Sedimentary Basin: Seismological Research Letters 87, 1-17.

Bao X., and Eaton D.W., 2016. Fault activation by hydraulic fracturing in western Canada: Science, *in press*. DOI: 10.1126/science.aag2583

B.C. Oil and Gas Commission, 2012. Investigation of Observed Seismicity in the Horn River Basin. Accessed from http://www.bcogc.ca/node/8046/download on 23.7.2015.

B.C. Oil and Gas Commission, 2014. Investigation of Observed Seismicity in the Montney Trend. Accessed from https://www.bcogc.ca/node/12291/download on 23.7.2015.

Chambers K., Kendall J-M., Brandsberg-Dahl S., Rueda J., 2010. Testing the ability of surface arrays to monitor microseismic activity: Geophysical Prospecting 58, 821-830.

Clarke H., Eisner L., Styles P., Turner P., 2014. Felt seismicity associated with shale gas hydraulic fracturing: The first documented example in Europe: Geophysical Research Letters 41, 8308-8314.

Clauset A., Shalizi C.R., Newman M.E.J., 2009. Power-law distributions in empirical data: Society for Industrial and Applied Mathematics Review 51, 661-703.

Darold A., Holland A.A., Chen C., Youngblood A., 2014. Preliminary analysis of seismicity near Eagleton 1-29, Carter County, July 2014: Oklahoma Geological Society Open File Report, OF2-2014.

Dinske C. and Shapiro S.A., 2013. Seismotectonic state of reservoirs inferred from magnitude distributions of fluid-induced seismicity: Journal of Seismology 17, 13-25.

Friberg P.A., Besana-Ostman G.M., Dricker I., 2014. Characterisation of an earthquake sequence triggered by hydraulic fracturing in Harrison County, Ohio: Seismological Research Letters 85, 1295-1307.

Gischig V.S., 2015. Rupture propagation behavior and the largest possible earthquake induced by fluid injection into deep reservoirs: Geophysical Research Letters 42, 7420-7428.

Gupta H.K., 1985. The present status of reservoir induced seismicity investigations with special emphasis on Koyna earthquakes: Tectonophysics 118, 257-279.

Gutenberg B. and Richter C.F., 1944. Frequency of earthquakes in California: Bulletin of the Seismological Society of America 34, 185-188.

521 Hajati T., Langenbruch C., Shapiro S.A., 2015. A statistical model for seismic hazard
522 assessment of hydraulic-fracturing-induced seismicity: Geophysical Research Letters 42,
523 10601-10606.

524 Hakimhashemi A.H., Schoenball M., Heidbach O., Zang A., Grünthal G., 2014. Forward
525 modelling of seismicity rate changes in georeservoirs with a hybrid geomechanical-
526 statistical prototype model: Geothermics 52, 185-194.

527 Hallo M., Oprsal I., Eisner L., Ali M.Y., 2014. Prediction of magnitude of the largest
528 potentially induced seismic event: Journal of Seismology 18, 421-431.

529 Häring M.O., Schanz U., Ladner F., Dyer B.C., 2008. Characterisation of the Basel 1
530 enhanced geothermal system: Geothermics 37, 469-495.

531 Keranen K.M., Savage H.M., Abers G.A., Cochran E.S., 2013. Potentially induced
532 earthquakes in Oklahoma, USA: Links between wastewater injection and the 2011 M_W 5.7
533 earthquake sequence: Geology 41, 699-702.

534 Langenbruch C. and Zoback M.D., 2016. How will induced seismicity in Oklahoma respond
535 to decreased saltwater injection rates? Science Advances 2, e1601542,

536 Li T., Cai M.F., Cai M., 2007. A review of mining-induced seismicity in China: International
537 Journal of Rock Mechanics and Mining Sciences 44, 1149-1171.

538 Maxwell S.C., Rutledge J., Jones R., Fehler M., 2010. Petroleum reservoir characterization
539 using downhole microseismic monitoring: Geophysics 75, A129-A137.

540 Maxwell S.C., Zhang F., Damjanac B., 2015. Geomechanical modeling of induced seismicity
541 resulting from hydraulic fracturing: The Leading Edge 34, 678-683

542 McGarr A., 2014. Maximum magnitude earthquakes induced by fluid injection: Journal of
543 Geophysical Research 119, 1008-1019.

544 Raleigh C.B., Healy J.H., Bredehoeft J.D., 1976. An experiment in earthquake control at
545 Rangely, Colorado: Science 191, 1230-1237.

546 Schultz R., Stern V., Novakovic M., Atkinson G., Gu Y.J., 2015a. Hydraulic fracturing and
547 the Crooked Lake sequences: Insights gleaned from regional seismic networks:
548 Geophysical Research Letters 42, 2750-2758.

549 Schultz R., Mei S., Pana D., Stern V., Gu Y.J., Kim A., Eaton D., 2015b. The Cardston
550 earthquake swarm and hydraulic fracturing of the Exshaw Formation (Alberta Bakken
551 play): Bulletin of the Seismological Society of America 105, 2871-2884.

552 Segall P., 1989. Earthquakes triggered by fluid extraction: Geology 17, 942-946.

553 Shapiro S.A., Dinske C., Langenbruch C., 2010. Seismogenic index and magnitude
554 probability of earthquakes induced during reservoir fluid stimulations: The Leading Edge
555 29, 304-309.

556 Skoumal R.J., Brudzinski M.R., Currie B.S., 2015. Induced earthquakes during hydraulic
557 fracturing in Poland Township, Ohio: Bulletin of the Seismological Society of America
558 105, 189-197.

559 Stork A.L., Verdon J.P., Kendall J-M. 2014. Assessing the effect of microseismic processing
560 methods on seismic moment and magnitude calculations: Geophysical Prospecting 62,
561 862-878.

562 Stork A.L., Verdon J.P., Kendall J-M., 2015. The microseismic response at the In Salah
563 carbon capture and storage (CCS) site: International Journal of Greenhouse Gas Control
564 32, 159-171.

565 van der Elst, N.J., Page M.T., Weiser D.A., Goebel T.H.W., Hosseini S.M., 2016. Induced
566 earthquake magnitudes are as large as (statistically) expected: Journal of Geophysical
567 Research 121, 4575-4590.

568 Verdon J.P., Stork A.L., Bissell R.C., Bond C.E., Werner M.J., 2015. Simulation of seismic
569 events induced by CO_2 injection at In Salah, Algeria: Earth and Planetary Science Letters
570 426, 118-129.

571 Verdon J.P., Kendall J-M., Hicks S.P., Hill P., 2017. Using beam-forming to maximise the
572 detection capability of broadband seismometer arrays deployed to monitor oilfield
573 activities: Geophysical Prospecting, *in press*.
574 Yoon J.S., Zang A., Stephansson O., 2014. Numerical investigation on optimized stimulation
575 of intact and naturally fractured deep geothermal reservoirs using hydro-mechanical
576 coupled discrete particles joints model: Geothermics 52, 165-184.
577 Wang R., Gu Y.J., Schultz R., Kim A., Atkinson G., 2016. Source analysis of a potential
578 hydraulic-fracturing-induced earthquake near Fox Creek, Alberta: Geophysical Research
579 Letters 43, 564-573.
580
581
582
583
584
585
586
587

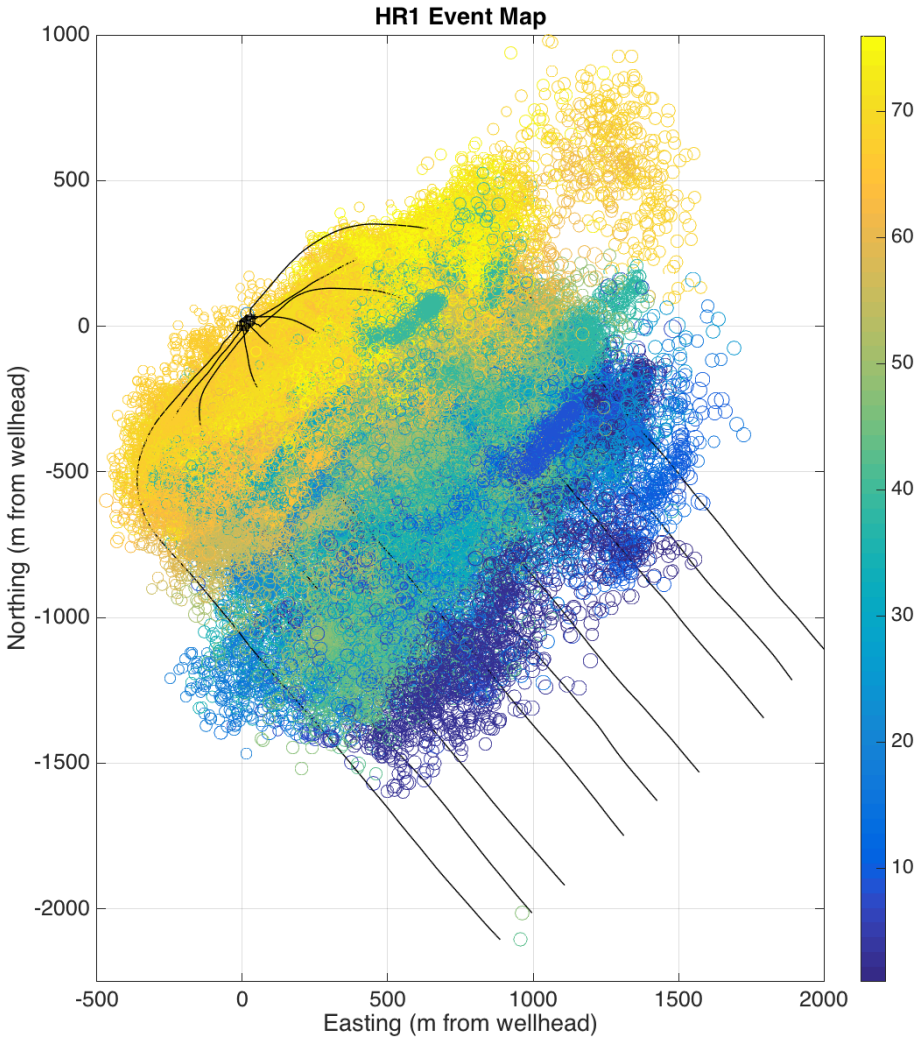

588

589 *(a)*

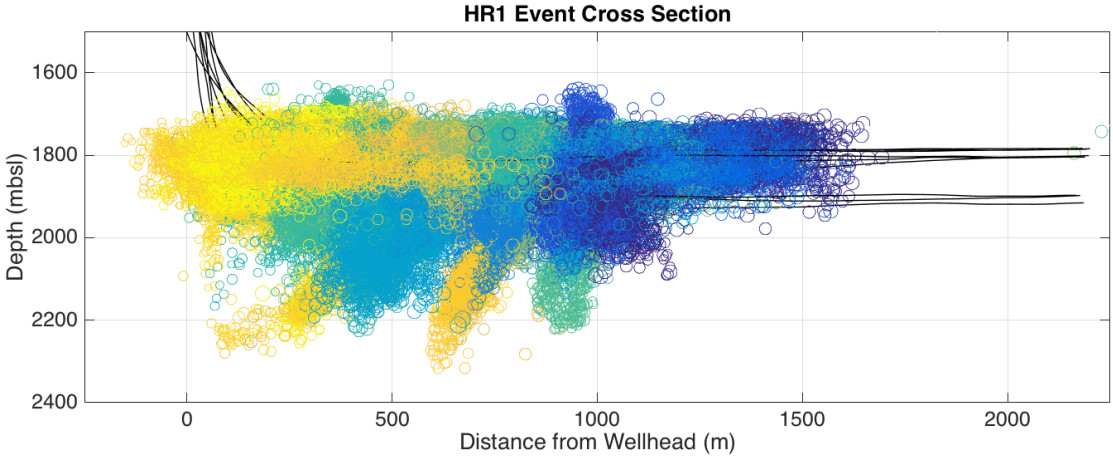

590

591 *(b)*

Figure 1: Map (a) and cross-section (b) views of microseismic events recorded during hydraulic fracturing at HR1. Events are coloured by the number of the stage with which they are associated. The black lines mark the horizontal wells.

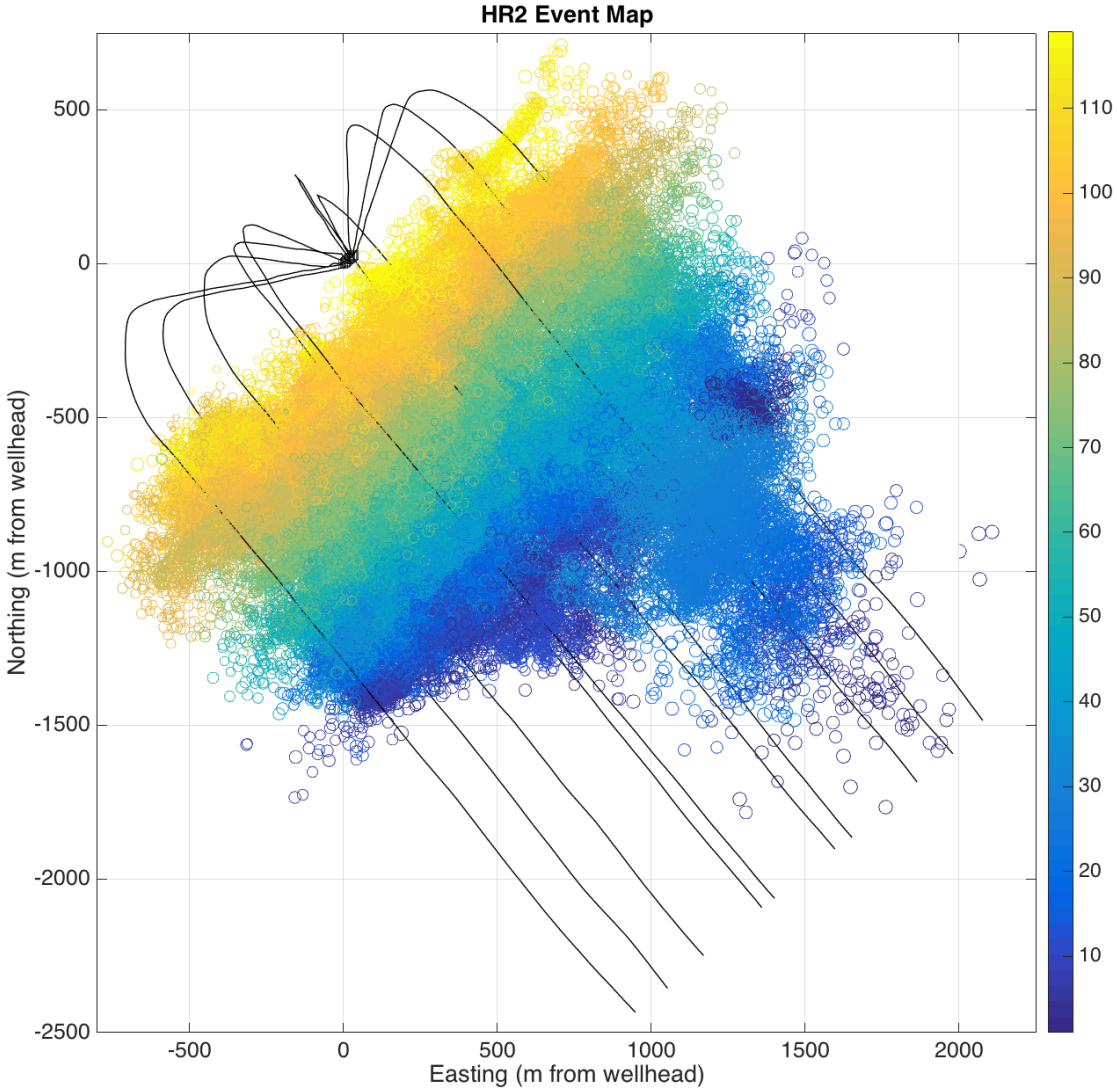

(a)

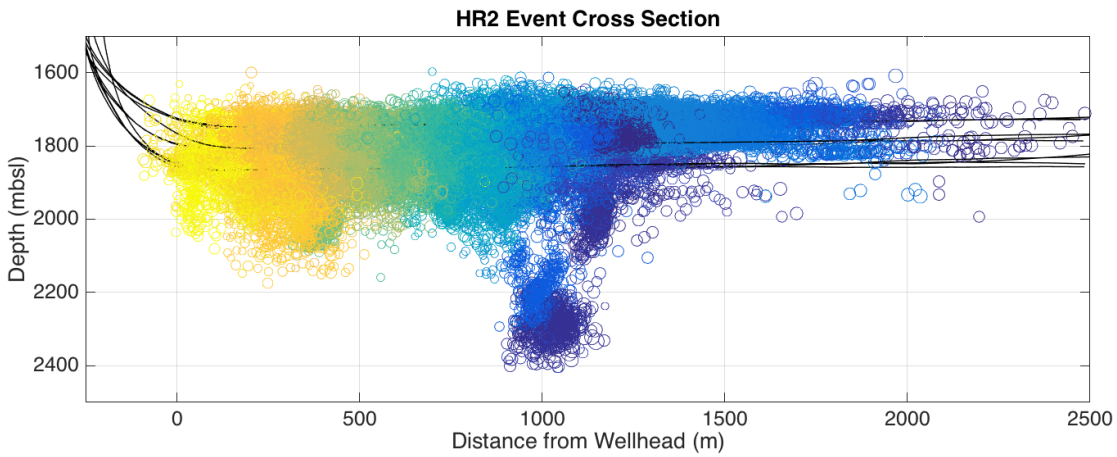

598 *(b)*

599 *Figure 2: Map (a) and cross-section (b) views of microseismic events recorded during hydraulic*
600 *fracturing at HR2. Events are coloured by the number of the stage with which they are associated. The*
601 *black lines mark the tracks of the horizontal wells.*

602

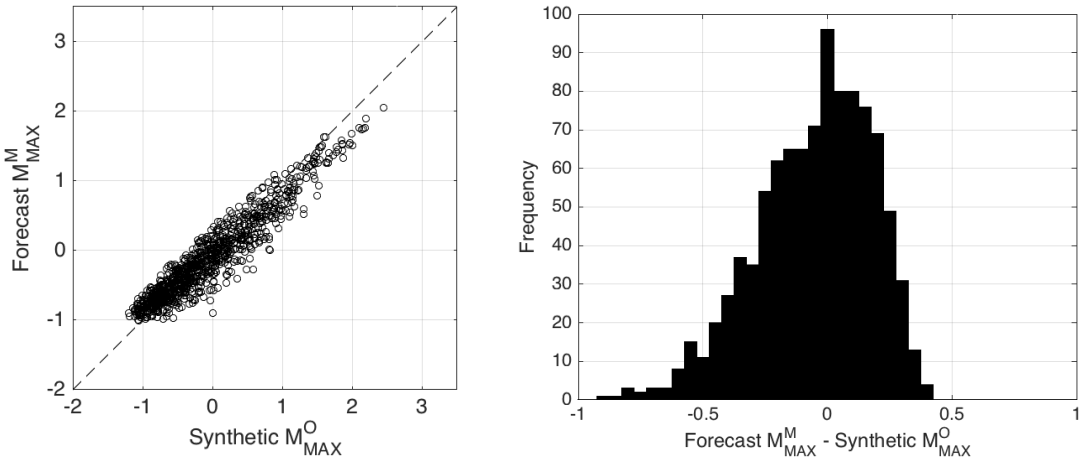

(a) *(b)*

603 *Figure 3: Numerical evaluation of the uncertainties inherent when using equations 6 and 7 to forecast*
604 *M_{MAX}. A modelled population of events is sampled from a G-R distribution. M_{MAX} is forecast, and*
605 *compared with the largest event in the simulated population. In (a) we compare the synthetic and*
606 *forecast values, while in (b) we show a histogram of the differences between the forecast and modelled*
607 *values.*

608

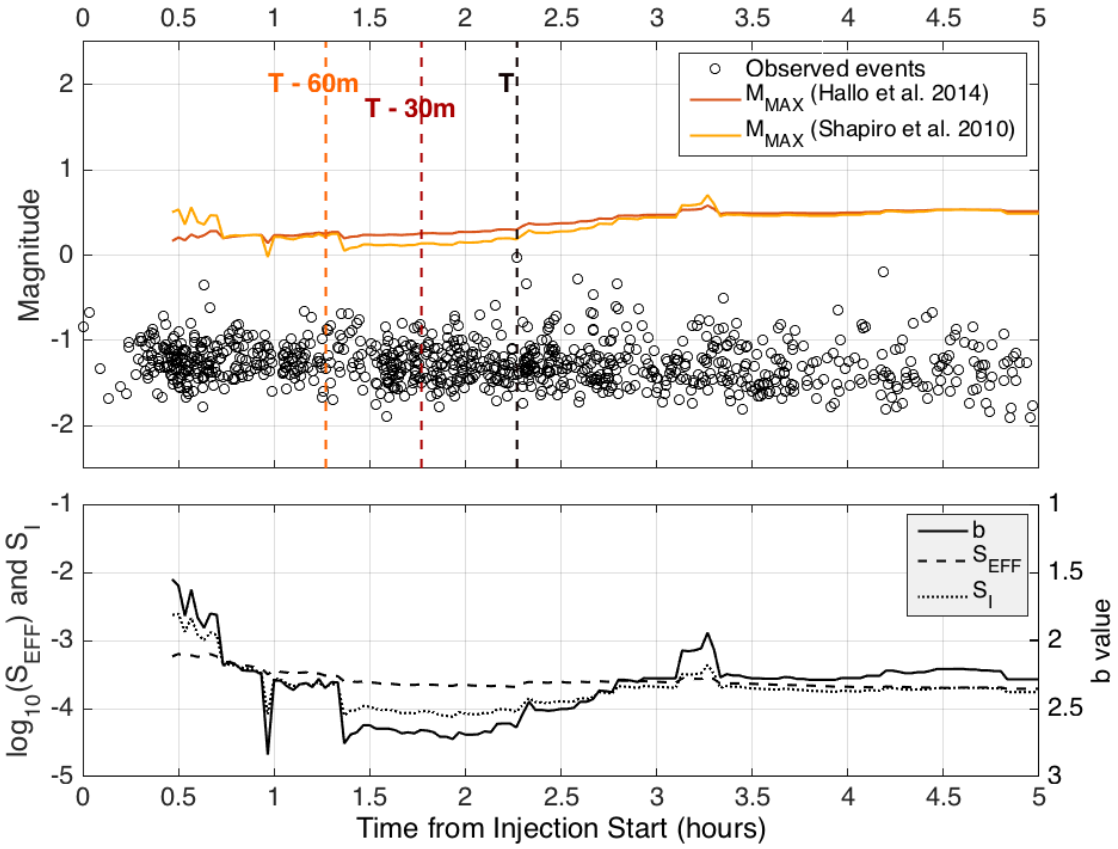

609

610 *Figure 4: Example demonstrating how we forecast M^{M}_{MAX} during a HF stage. In the lower panel we*
611 *update b, S_{EFF} and S_I during injection. Based on these parameters, we estimate M^{M}_{MAX} using the*
612 *methods described by Shapiro et al. (2010) and Hallo et al. (2014), and compare these to the observed*
613 *event population. The vertical dashed lines in the upper panel represent the M^{M}_{MAX} estimates at the*
614 *time of the largest event, and 30 and 60 minutes prior to this event. This data is from stage HR1-A-S10.*

615

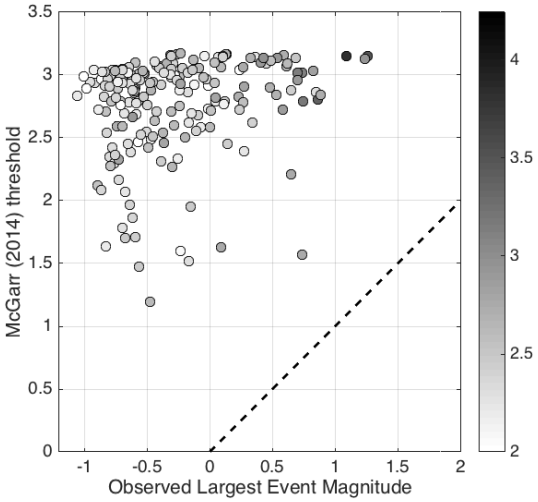

616

Figure 5: Comparison between the observed M^{O}_{MAX} for every stage of both datasets, and that estimated using the McGarr (2014) equation, where M^{M}_{MAX} is directly determined by the injected volume. Symbols are coloured by $log_{10}(N)$, where N is the total number of events per stage. The dashed line indicated a 1:1 ratio.

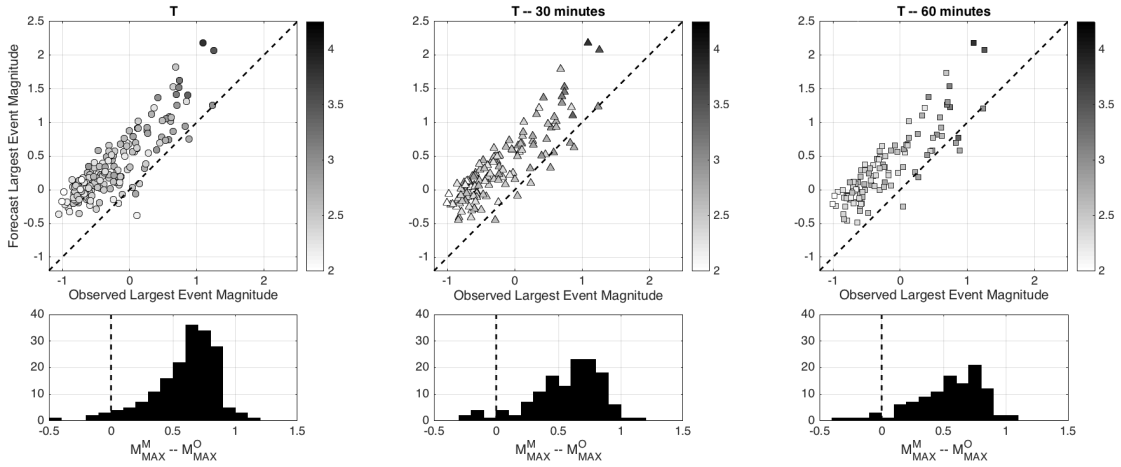

Figure 6: Comparison between the observed M^{O}_{MAX} for every stage of both datasets, and that estimated using the Hallo et al. (2014) approach. The upper panels show crossplots of observed and modelled M^{M}_{MAX} values, while the lower panels show histograms of M^{M}_{MAX} - M^{O}_{MAX}. For each case we show the values of M^{M}_{MAX} at the time that the largest event occurred, and at 30 and 60 minutes prior to this time. The symbols are coloured by $log_{10}(N)$, where N is the total number of events per stage. The dashed lines in the upper panels represent $M^{O}_{MAX} = M^{M}_{MAX}$. Note that for a handful of stages, robust estimates are only obtained within 30 or 60 minutes of the largest event. In such cases, no M^{M}_{MAX} value is returned at the T – 30 or T – 60 cases, and so there are slightly fewer points plotted for these cases.

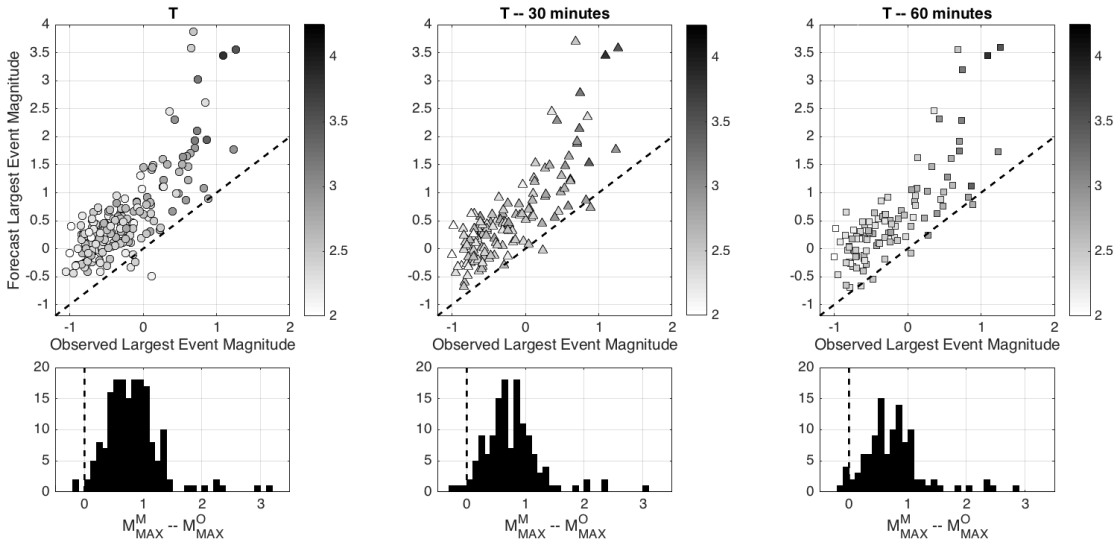

632

633 *Figure 7: Comparison between the observed M^O_{MAX} for every stage of both datasets, and that estimated*

634 *using the Shapiro et al. (2010) approach. This figure follows the same format as Figure 6.*

635

636

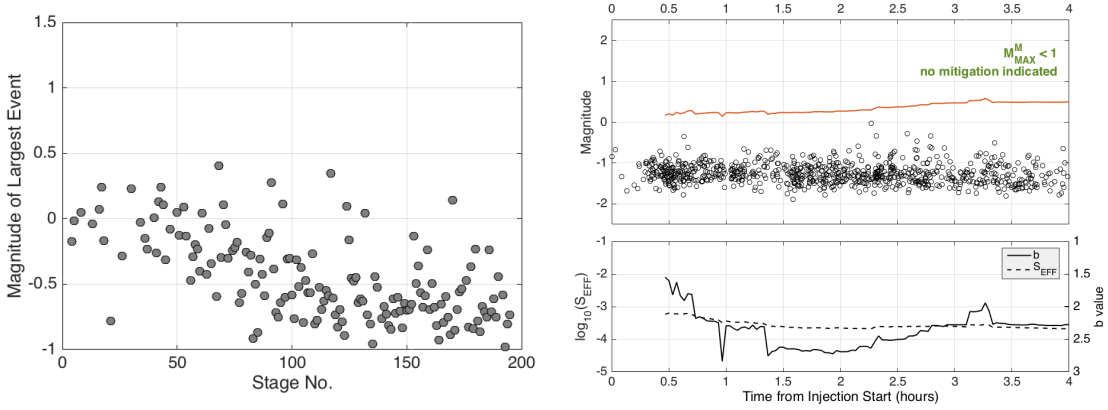

(a) *(b)*

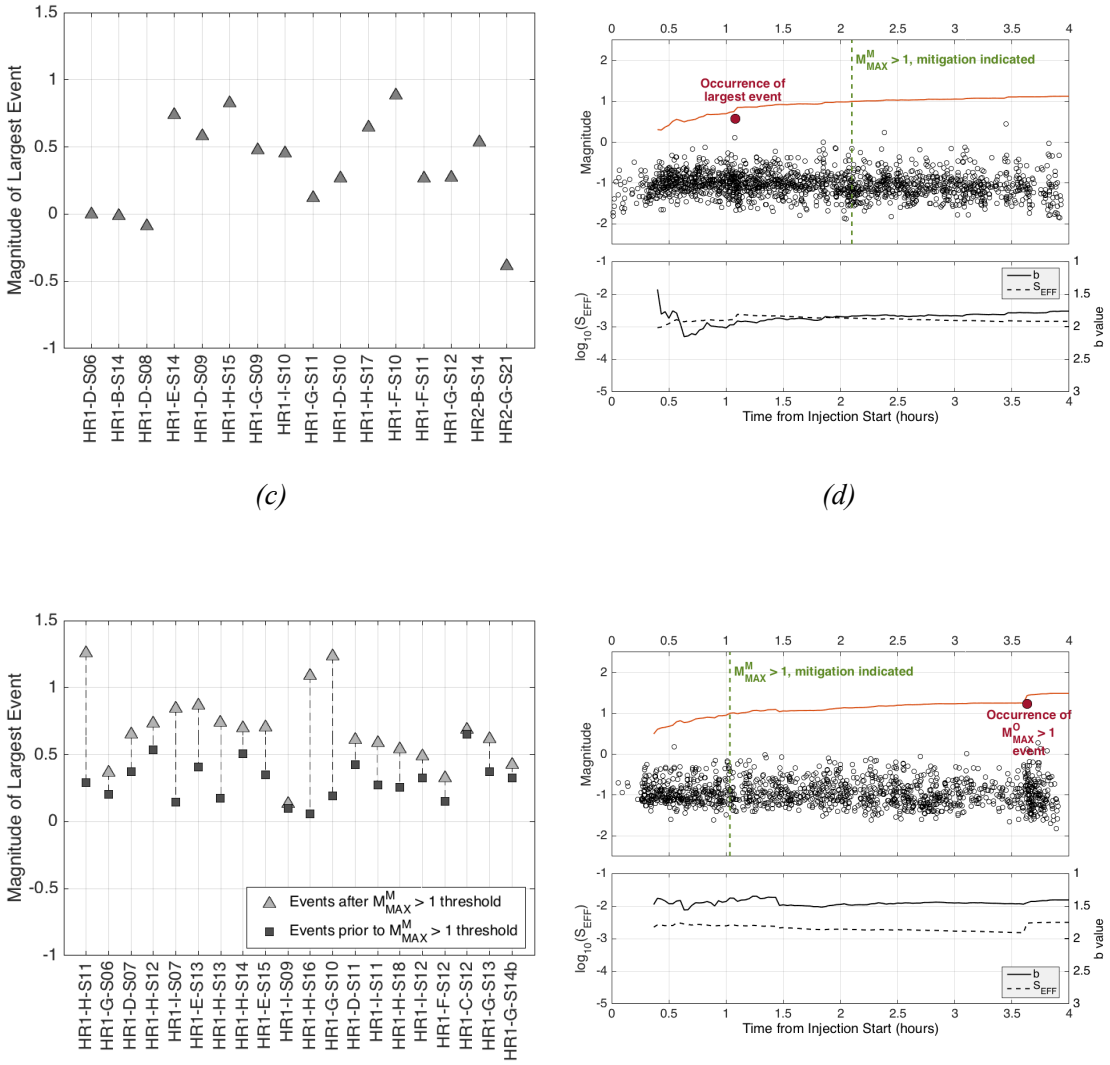

637 *Figure 8: Testing the ability of the proposed approach to mitigate induced seismicity. In (a) we show*
638 M^{O}_{MAX} *for each stage that did not reach the* $M^{M}_{MAX} > 1$ *threshold. An example of such a stage, where*
639 *no mitigation actions would have been taken, is shown in (b). In (c) we show* M^{O}_{MAX} *for each stage that*
640 *reached the mitigation threshold, but only after the largest event had occurred. In such cases, any*
641 *mitigation steps would not affect* M^{O}_{MAX} *(since the largest event has already occurred). In (d) we show*
642 *an example of such a stage. In (e) we show* M^{O}_{MAX} *for each stage that reached the* $M^{M}_{MAX} > 1$ *threshold*
643 *prior to the occurrence of* M^{O}_{MAX}*. The triangles show the values of* M^{O}_{MAX} *that actually occurred. The*
644 *squares show the largest event that had occurred prior to reaching the threshold. In (f) we show an*
645 *example of such a stage.*

646